Shock Wave Induced Decomposition of RDX: Quantum Chemistry Calculations

Maosheng Miao, Zbigniew A. Dreger,* James E. Patterson, and Yogendra M. Gupta

Institute for Shock Physics and Department of Physics, Washington State University, Pullman, Washington 99164-2816

Received: January 28, 2008; Revised Manuscript Received: April 21, 2008

Quantum chemical calculations on single molecules were performed to provide insight into the decomposition mechanism of shocked RDX. These calculations complement time-resolved spectroscopy measurements on shock wave compressed RDX crystals (previous paper, this issue). It is proposed that unimolecular decomposition is the primary pathway for RDX decomposition in its early stages and at stresses lower than ~10 GPa. This decomposition leads to the generation of broadband emission from 350 to 850 nm. Chemiluminescence from $^2B_1$ and $^2B_2$ excited states of NO_2 radicals is associated with a major portion of the experimentally observed emission spectrum (>400 nm). The remaining portion (<400 nm) of the emission spectrum primarily results from excited HONO intermediates. It is proposed that for stresses higher than 10 GPa, bimolecular reactions between radical decomposition products and unreacted RDX molecules become the dominant pathway. This radical assisted homolysis pathway is cyclic and leads to the acceleration of decomposition, with increased production of low energy NO_2 radicals. These radicals produce emission that is stronger in the long wavelength portion of the spectrum. Finally, a comprehensive chemical decomposition mechanism is put forward that is consistent with the experimental observations of shock-induced emission in RDX crystals.

I. Introduction

In our companion paper,[1] time-resolved emission spectroscopy measurements were used to identify several key features of the shock induced decomposition of RDX. First, we observed a threshold in the response of RDX at about 10 GPa. Below this stress, decomposition leads to multiple products that give rise to a broad emission spectrum. Three spectral components were distinguished: wavelengths less than 400 nm (UV); visible wavelengths (VIS), from 400 to about 650 nm; and long wavelengths (LW), to our detection limit of 850 nm. The LW component was tentatively assigned to NO_2, which may also be the source of the VIS component. We also suggested that HONO could be the source of the UV emission.

At peak stresses above 10 GPa, the spectral profile initially resembled that of the lower stress experiments. The profile changed with time, however, until the LW component dominated the spectrum. Greater production of NO_2, through a different decomposition pathway, was suggested as the reason for this spectral change. The reaction also appeared to accelerate at higher stresses, as indicated by the significant increase in total emission intensity. We proposed that bimolecular reactions between radical decomposition intermediates and RDX molecules become the dominant decomposition channel above the 10 GPa threshold.

Here, we use quantum chemical calculations on single molecules to develop a qualitative decomposition scheme for shock wave compressed RDX. Excited-state calculations were used to identify the emitting species which are the possible reaction intermediates. Activation barriers and transition states for candidate reactions were determined using quantum chemistry calculations.

Considerable work has been done by other researchers to apply computational techniques to RDX decomposition.[2–11] Although most studies focused on the first decomposition step, more extensive pathways have also been examined.[2,9] As reviewed in our companion paper,[1] these computational efforts were carried out in the context of prior experimental work, which did not emphasize shock wave experiments. Thus, it is not clear if the inferences from these earlier experiments are applicable to shock-induced decomposition.

The remainder of this paper is organized as follows. Computational methods are discussed in section II. Results

TABLE 1: Transition Energies and Oscillator Strengths for Low-Lying Excited States of Selected Intermediates of RDX Decomposition[a]

	CIS		TDDFT	
	1st state	2nd state	1st state	2nd state
HONO	3.39	3.99	3.03	3.17[b]
	(366)	(311)	(402)	(391)
	0.0033	0.0003	0.0010	0.0003
N_2O	0.37	5.25	0.92[b]	5.38
	(3346)	(236)	(1354)	(231)
	0.0000	0.0010	0.0000	0.0000
NO	0.26	5.65	0.01	4.87
	(4752)	(219)		(255)
	0.0000	0.0042	0.0000	0.0040
CH_2N	4.79	5.17	4.56[b]	5.48
	(259)	(240)	(272)	(226)
	0.0113	0.0000	0.0062	0.0002
HCN	3.58	5.43	4.40	5.42
	(346)	(228)	(282)	(229)
	0.0019	0.0100	0.0028	0.0101
CH_2O	4.09	7.88	3.46[b]	6.53[b]
	(303)	(157)	(358)	(190)
	0.0006	0.1203	0.0005	0.0885

[a] In each cell, the first number is the transition energy in electronvolts, the number in parentheses is in nanometers, and the last number is the corresponding oscillator strength. [b] Using CIS geometry.

* Corresponding author. E-mail: dreger@wsu.edu.

10.1021/jp8008282 CCC: $40.75
Published on Web 07/22/2008

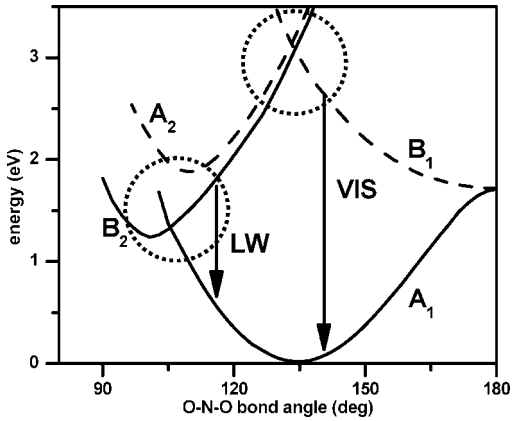

Figure 1. Potential energy surfaces of the ground and first three excited states of NO_2 (after refs 21 and 22). Circled areas show mixing between A_1:B_2 and B_1:A_2 states. Vertical arrows indicate characteristic emission from the B_2 and B_1 states.

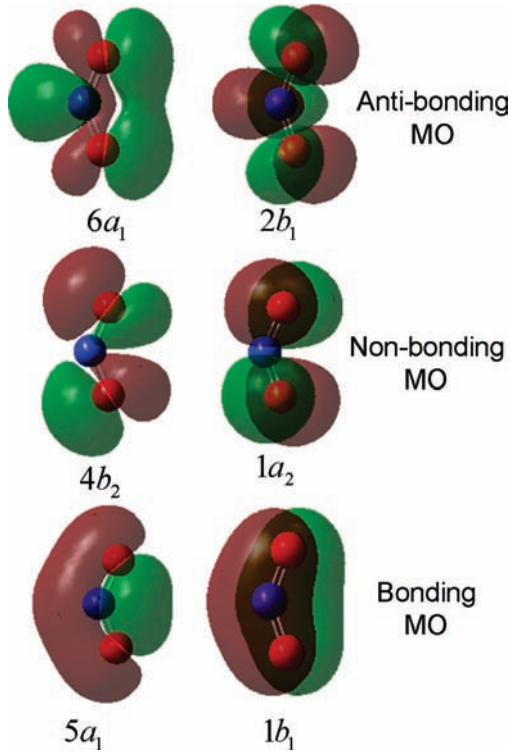

Figure 2. Molecular orbitals of NO_2. Orbitals were calculated at the B3LYP level of DFT with the 6-311+G(d,p) basis set. The numbering of the different symmetry states takes into account the lower lying σ orbitals. The $5a_1$, $1b_1$, $4b_2$, and $1a_2$ orbitals are fully occupied, $6a_1$ is partially occupied and $2b_1$ is unoccupied.

of the electronic structure calculations and the identification of the emitting species are presented in section III. Section IV presents chemical reaction calculations and the comprehensive decomposition scheme. Concluding remarks are presented in section V.

II. Computational Approach

To develop a qualitative decomposition scheme compatible with shock wave experiments on RDX crystals,[1] we performed calculations on the excited states of various decomposition intermediates and chemical reaction pathways for isolated molecules. Despite this obvious simplification, we believe that this approach provides useful guidance and insight into the decomposition processes in the shocked crystal.

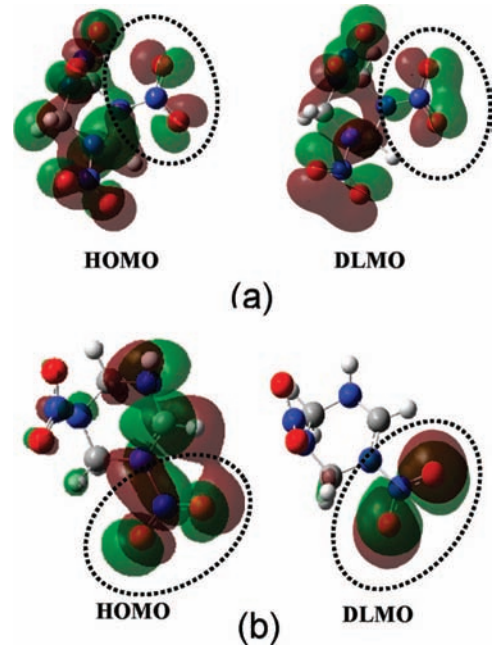

Figure 3. Selected molecular orbitals of (a) RDX and (b) RDR-C. DLMO = deep level molecular orbital. Orbitals were calculated at the B3LYP level of DFT with the 6-311+G(d,p) basis set.

The excited-state properties of likely decomposition intermediates, including vertical transition energies to the ground-state and oscillator strengths, were calculated using the configuration interaction singlet (CIS) method and time-dependent density functional theory (TDDFT) with the 6-311+G(d,p) Gaussian basis set. A large Gaussian basis set with diffuse functions was needed because of the delocalization of the wave functions of the excited states. The CIS approach provides reliable geometries for the excited states of these small molecules, but the energy level calculations are not as accurate. TDDFT gives better results for the excited-state energies, but the geometry is optimized by numerically calculated forces. This method did not always successfully determine the equilibrium geometry of the excited states, and in these cases, the CIS geometry was used for the TDDFT energy calculation.

Chemical reaction pathways were studied by calculating the geometries and energies of the reactants, products and transition states. We employed the density functional theory (DFT) approach with the Becke three-parameter exchange functional and Lee−Yang−Parr nonlocal correlation functional (B3LYP)[14–17] with the 6-311+G(d,p) Gaussian basis set. For stationary states, all calculated vibrational frequencies were positive. Transition states had only one imaginary frequency. We did not include zero point effects (ZPE) in our results because such effects were determined to be minor in the decomposition reactions of RDX. All calculations were performed with the Gaussian 03 computation package.[18]

Again, all calculations were performed on isolated molecules. It is possible that the crystal environment has some effect on decomposition reactions and radiative transitions. However, the bond length of RDX molecules in the crystal changes only slightly under compression. For example, the average N−N bond length of γ-RDX at 5.2 GPa[12] is about 1.35 Å, which is only 4% smaller than the 1.41 Å bond length observed in the gas phase.[13] We also examined solution effects on the transition energies and the oscillator strengths of selected emitting intermediates and found negligible changes regardless of the solution model or the dielectric constant used in the calculation.

The effect of shock conditions, i.e., pressure and temperature, on the decomposition can be more important than the effect of crystal environment. It is, however, believed that these conditions will not significantly alter the preference of decomposition pathways.

III. Identification of Decomposition Intermediates

Excited-State Calculations. We calculated vertical transition energies from the excited states to ground states, and the corresponding oscillator strengths, for several possible early decomposition intermediates. Our goal was to identify the source of the VIS and UV components of the emission spectrum.[1] The results of the CIS and TDDFT calculations for selected, potential intermediates are presented in Table 1. NO_2 is not included in this table because it is discussed in detail in the next section.

The excited-state calculations identify HONO as a possible source of the UV component of the emission, as suggested previously.[1] HONO elimination is one of three primary decomposition channels proposed for RDX.[9] Its production in early stages of decomposition is consistent with experimental observations and mechanistic considerations. Because the HONO emission is close to the absorption edge of RDX around 350 nm, some of the light emitted by this species is probably not observable, as discussed previously.[1] Another possible source of UV emission is NO. Emission from its β band ranges from 200 to 650 nm, with a peak at around 340 nm. However, there is a lack of reaction pathways that can generate NO at the early stage of decomposition. HONO can dissociate into NO and OH radicals, but this usually occurs at higher temperatures than are attained in our shock experiments.

The VIS component of the emission spectrum covers a range of wavelengths from about 400 to 650 nm, or energies from 2 to 3 eV. As shown in Table 1, none of the decomposition fragments has a vertical transition in this range. Similar results were found for other molecules not included in Table 1. One transition, from the second excited state of CHO, can emit light at around 450 nm, but CHO is unlikely as an early stage intermediate of RDX decomposition. Furthermore, the HONO and NO emission can overlap with the VIS region of the spectrum. However, because their emission peaks are outside the VIS region, they are unlikely to be major sources for this component. Therefore, NO_2 is the most likely source of both the VIS and LW emission components. Because these emission components have different temporal behavior, there must be a mechanism for NO_2 to emit light through two different transitions.

Electronic Structure of NO_2. Excited NO_2 molecules are known to produce a broad, almost continuous, emission spectrum from 390 nm to near-infrared.[19] In addition, the spectral profile depends on how NO_2 is produced.[20] Figure 1 depicts the potential energy surfaces (PES) of NO_2, based on the work of Gillispie and Khan.[21,22] NO_2 exhibits three low lying excited states, labeled B_1, A_2 and B_2, in addition to the A_1 ground state. Because NO_2 is a radical, these are spin doublet states. The N−O bond lengths are optimized for each excited state in this plot. The ONO bond angle is optimized at 133° in the ground state, which is close to the ONO bond angle in RDX of ∼125°.

Excited states of NO_2 are known to have long lifetimes, which are attributed to coupling between the various vibronic states.[23] If one allows for asymmetric distortion of the NO_2 molecule, the symmetry reduces from C_{2v} to C_s. In the C_s point group, the A_1 and B_2 terms both become A′ and the A_2 and B_1 terms become A. Thus, there is strong coupling between the A_1 and B_2 states and the A_2 and B_1 states. Mixing between the vibronic states of the $^2A_1$ ground state and the $^2B_2$ excited state is very strong.[24,25] If NO_2 is produced in the B_2 state, this coupling can lead to emission over a broad range of wavelengths, with larger intensity at long wavelengths. The transition $^2A_1 \leftarrow {}^2A_2$ is dipole forbidden; however, mixing of the A_2 and B_1 states will allow for emission from the B_1 state. This mixing leads to longer lifetimes near the intersection of these states and produces emission at higher energies than from the B_2 state. Thus, it appears reasonable that the LW component of the emission is produced by the $^2A_1 \leftarrow {}^2B_2$ transition and the VIS component from the $^2A_1 \leftarrow {}^2B_1$ transition. A mechanism is still needed to populate these different excited states.

Linear triatomic molecules have three π molecular orbitals, one bonding, one nonbonding and one antibonding, that are important for this discussion. NO_2 has a bent geometry, which causes each of these three orbitals to split into two, as shown in Figure 2. Molecular orbitals were calculated at the B3LYP level of DFT with the 6-311+G(d,p) basis set. The π electronic configuration of the ground and excited states of NO_2 can be written as follows:

$$^2A_1 \quad 5a_1^{\,2}1b_1^{\,2}4b_2^{\,2}1a_2^{\,2}6a_1^{\,1}2b_1^{\,0}$$

$$^2B_2 \quad 5a_1^{\,2}1b_1^{\,2}4b_2^{\,1}1a_2^{\,2}6a_1^{\,2}2b_1^{\,0}$$

$$^2A_2 \quad 5a_1^{\,2}1b_1^{\,2}4b_2^{\,2}1a_2^{\,1}6a_1^{\,2}2b_1^{\,0}$$

$$^2B_1 \quad 5a_1^{\,2}1b_1^{\,2}4b_2^{\,2}1a_2^{\,2}6a_1^{\,0}2b_1^{\,1}$$

For example, for the ground state of NO_2, the $5a_1$, $1b_1$, $4b_2$ and $1a_2$ orbitals are fully occupied, $6a_1$ is half-filled, and $2b_1$ is unoccupied.

Next, we consider the electronic structure of the NO_2 group of RDX. The molecular orbitals of a single ground-state RDX molecule were calculated for the axial-axial−equatorial (AAE) conformer that exists in the crystalline phase.[26] Figure 3a shows the highest occupied molecular orbital (HOMO) and another deep level molecular orbital (DLMO) that lies about 1.2 eV below the HOMO. Orbitals between these two are not considered because they do not have sufficient electron density localized on the NO_2 group. Comparison of the orbitals in Figure 3a with those in Figure 2 indicates that the HOMO wave function around the nitro group resembles the $4b_2$ state of NO_2. The DLMO wave function, however, resembles the $6a_1$ state of NO_2. Thus, for the NO_2 group of RDX, the order of the $4b_2$ and $6a_1$ states is reversed in terms of energy. If we assume that the electronic configuration does not change during bond breaking, homolytic cleavage of the N−N bond will produce NO_2 with the electronic configuration of $5a_1^{\,2}1b_1^{\,2}4b_2^{\,1}1a_2^{\,2}6a_1^{\,2}2b_1^{\,0}$, which describes the $^2B_2$ excited state. The ground state of RDX connects with an excited state of NO_2, whereas the ground state of NO_2 connects to an excited state of RDX. This crossing of states suggests a small energy gap between the ground and excited states of NO_2 along the N−N homolysis reaction. If the radiative transition occurs before any nonradiative processes, NO_2 in the $^2B_2$ excited state can generate LW emission. Coupling between the A_1 ground state and the B_2 excited state may aid this process and extend the lifetime of the excited state.[22]

The reordering of the $4b_2$ and $6a_1$ orbitals is caused by the coupling between the nitro group and the ring. Although $6a_1$ is an antibonding state in free NO_2, the portion of this wave function on the N atom can couple with the N atom on the triazine ring, lowering the energy of this orbital. On the other hand, the $4b_2$ orbital of NO_2 is nonbonding and has a node on

the N atom; its coupling with the ring is very weak. We can extend the above argument to other molecules. For example, calculations for methylene nitramine (CH_2NNO_2) also show the reordering of the $4b_2$ and $6a_1$ states. Therefore, homolysis of the N−N bond of CH_2NNO_2 can also lead to the production of NO_2 in the $^2B_2$ state, which can result in LW emission.

During RDX decomposition, other intermediates can also eliminate NO_2 through N−N homolysis. One such species is a C-centered radical produced by the elimination of a single NO_2 group and the migration of hydrogen to the N radical center. This radical is labeled RDR-C and is depicted in the Appendix, along with several other decomposition products. The HOMO of RDR-C is half-filled and the wave function around the nitro group resembles the $2b_1$ state of NO_2. The HOMO and a lower lying orbital are depicted in Figure 3b. For this DLMO of RDR-C, the wave function around the nitro group resembles the $1a_2$ state of NO_2. Again, interactions with the ring lead to a reordering of the NO_2 orbitals; the $6a_1$ orbital lies below the $4b_2$ and $1a_2$ orbitals, and the latter two states differ in energy by about 0.1 eV. Our calculations indicate that during N−N homolysis, the $1a_2$ orbital becomes higher in energy than the $4b_2$ state, suggesting that the ground state of RDR-C connects to the $^2A_2$ excited state of NO_2. Coupling between the $^2A_2$ and $^2B_1$ states can give rise to the transition $^2A_1 \leftarrow {}^2B_1$ producing VIS emission.

The type of emission will also depend on the amount of energy released to the reaction products during homolysis. Because N−N homolysis from a nonradical molecule leads to the production of two radical products, this process is typically endothermic. The product state is of higher energy than the reactant state. NO_2 produced in this fashion is therefore likely to have low internal energy. On the other hand, a radical such as RDR-C already has considerable chemical energy, and its release of NO_2 produces a stable molecule and a small radical. The products are of lower energy than the reactant. This suggests that the NO_2 produced from a C-radical should have more internal energy and could emit light at shorter wavelengths than NO_2 produced from a nonradical molecule.

On the basis of the molecular orbital and chemical reaction considerations presented here, we can attribute both the VIS and LW components of the emission spectrum to NO_2. When NO_2 is produced by N−N homolysis from a nonradical molecule, it occurs preferentially in the B_2 excited state and can give LW-type emission. However, if NO_2 is eliminated from a C-centered radical, it can be produced in the A_2 excited states with higher internal energy and can give VIS emission.

IV. RDX Decomposition Mechanism

Criteria for Proposed Decomposition Scheme. The foregoing discussion identified the emitting species in the shock-induced decomposition of RDX. On the basis of these results, the early stage of decomposition should lead to production of HONO and NO_2. NO_2 is produced through two separate reaction channels that give rise to the VIS and LW emission components. The LW emission component comes from NO_2 eliminated by a nonradical molecule and the VIS component originates from NO_2 eliminated by a C-centered radical. The experiments also identified a threshold above which decomposition accelerates, generating stronger LW emission.

A proposed decomposition scheme is outlined in Figure 4. Reaction pathway calculations are used to check the plausibility of particular chemical reactions. The structures of various decomposition products and intermediates are shown in the Appendix. The details of this scheme will be presented in following sections.

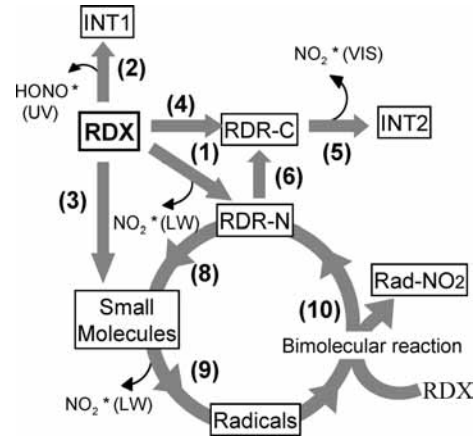

Figure 4. Proposed scheme of shock-wave induced decomposition of RDX crystal.

Initial Decomposition Step. Three major reaction channels have been proposed[27] for RDX: N−N homolysis, HONO elimination, and concerted ring fission.

$$\mathrm{RDX} \rightarrow \mathrm{RDR\text{-}N} + \mathrm{NO_2} \quad (1)$$

$$\mathrm{RDX} \rightarrow \mathrm{INT1} + \mathrm{HONO} \quad (2)$$

$$\mathrm{RDX} \rightarrow 3\mathrm{CH_2NNO_2} \quad (3)$$

Activation barriers for these pathways were calculated previously for gas phase RDX.[7,9] These calculations were done for the triaxial (AAA) conformer, but not for the AAE conformer known to exist in the solid state. AAE is also considered to be the conformation of RDX in the high pressure γ-phase.[28,29]

The results of our calculations for the AAE conformer of RDX are shown in Table 2. To compare these with previous results, and to examine the effects of molecular conformation, we also calculated the energy barriers of both conformations with the 6-31G(d) Gaussian basis set, used in a previous study.[9] Our results using this basis set agree with those of ref. Nine to within 5−10%. The effect of molecular conformation was negligible. The larger basis set 6-311+G(d,p) lowers activation barriers for all three channels by about 5%. This level of theory was used for the remaining calculations. The activation barriers for the homolysis, HONO, and ring fission pathways are 38.9, 42.4, and 63.0 kcal/mol, respectively.

The activation barriers for the N−N homolysis and HONO elimination pathways are very similar, suggesting that both take place in early RDX decomposition. The triple ring fission pathway appears to be less likely in early decomposition because of the large activation barrier. In addition, the large positive activation volume hinders this process in the solid state.[30]

Decomposition at Low Stress. We propose that reactions 1 and 2 are the dominant channels in the initial decomposition of RDX. Generation of HONO leads to the production of the UV emission observed early in the shocked crystal. Intermediate INT1, however, is relatively stable and does not participate further in our decomposition scheme.

Reaction 1 leads to the production of NO_2 and a N-centered radical, labeled RDR-N. Reaction 1 has an activation barrier of 38.9 kcal/mol as shown in Figure 5, but there is no net energy release upon completion of this reaction. The first step in the decomposition of an energetic material is often endothermic.[31] Thus, the NO_2 and the RDR-N radical may recombine before undergoing further decomposition, which may be more likely

TABLE 2: Activation Barriers for the First Decomposition Step of RDX from DFT Calculations for Different Basis Sets and RDX Conformers (All Energies in kcal/mol)

	B3LYP6-311+G(d,p) AAE	B3LYP6-31+G(d) AAE	B3LYP6-31+G(d) AAA	B-PW91D95V AAA[a]	B3LYP6-31+G(d) AAA[b]
N−N homolysis	38.9	41.1	41.6	34.2	39.0
HONO elimination	42.4	44.2	43.8		39.2
triple ring scission	63.0	64.6	64.4	52.5	59.4

[a] From ref 7. [b] From ref 9.

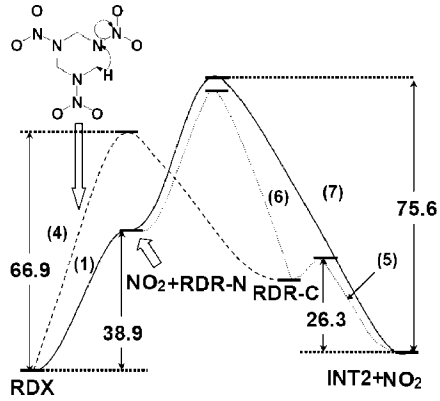

Figure 5. Potential energy profiles for NO_2 elimination reactions from RDX and RDX radicals without ring opening. Energy given in kcal/mol.

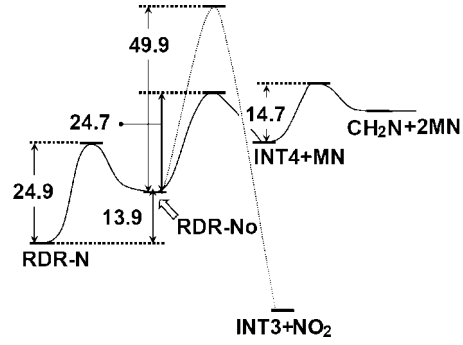

Figure 6. Potential energy profiles for RDR-N ring opening and subsequent reactions. Energy given in kcal/mol.

in the solid state. If emission occurs prior to recombination, NO_2 produced in this way could contribute to the LW portion of the emission spectrum.

As discussed above, the VIS emission component arises through NO_2 elimination from RDR-C. We propose concerted elimination of NO_2 and H migration from a C to N site as a pathway from RDX to RDR−C, reaction 4.

$$\text{RDX} \rightarrow \text{RDR-C} + \text{NO}_2 \tag{4}$$

Reaction 5 leads to the observed VIS emission

$$\text{RDR}-\text{-C} \rightarrow \text{INT2} + \text{NO}_2 \tag{5}$$

RDR-C can also be produced from RDR-N through H migration.

$$\text{RDR-N} \rightarrow \text{RDR-C} \tag{6}$$

The activation barrier for reaction 4 is calculated to be 66.9 kcal/mol, which is considerably greater than the barrier for the N−N homolysis in reaction 1. However, this barrier is lower than the total barrier for reaction 1 followed by reaction 6. Examination of the vibrational modes of RDX indicates strong coupling between the C−H wagging modes and the N−N stretching modes. This coupled motion may increase the pre-exponential factor for reaction 4. Unlike direct N−N homolysis, this reaction also exhibits a large back barrier. RDR-C, produced by either path, will readily eliminate NO_2 because the barrier for reaction 5 is only 3.1 kcal/mol. All these pathways are depicted in Figure 5.

In addition to reaction 6, RDR-N can eliminate another NO_2, with concerted migration of H from C to a ring N, to produce INT2.[9]

$$\text{RDR-N} \rightarrow \text{INT2} + \text{NO}_2 \tag{7}$$

This is the same product as produced in reaction 5; however, the barrier for reaction 7 is slightly larger than for reaction 6, indicating some preference for the two-step process.

These calculations also support the trend discussed earlier regarding the energetics of NO_2 elimination reactions. When NO_2 is produced from a nonradical molecule, such as RDX, it gains little excess energy from the reaction. NO_2 from a C-centered radical, however, should have significantly more internal energy. The back barrier for elimination from RDR-C is ∼1 eV. NO_2 produced from a N-centered radical should have even more internal energy, as indicated by the back barrier of ∼ 3 eV for elimination from RDR-N. However, as we show in the next section, reaction 7 is less likely than ring opening reactions.

Ring Opening Reactions. Except for reaction 3, the preceding reactions all occur without opening of the triazine ring. An alternate channel for the further decomposition of RDR-N and RDR-C involves ring opening. This pathway was calculated for both species. For RDR-N, the barrier to ring opening is 24.9 kcal/mol, which is smaller than the barrier for both reactions 7 and 6. Thus, it appears that ring opening is a favorable decomposition channel for RDR-N. RDR-C, however, is more likely to eliminate NO_2 than to undergo ring opening; the activation barriers are 3.1 and 21.8 kcal/mol, respectively. Thus, RDR-N is the most likely species to undergo ring opening during this stage of the decomposition. Figure 6 depicts the ring opening and subsequent decomposition pathways for RDR-N. The ring-opened radical is labeled RDR-No.

Upon ring opening, RDR-No can react in several different ways. First, it can eliminate NO_2, accompanied by H migration, to produce INT3. The barrier for NO_2 elimination is 49.9 kcal/mol, similar to reaction 7. It can also undergo H migration to form a C-centered radical. A H migration pathway was previously proposed[9] but seems unfavorable on the basis of steric constraints, particularly in the condensed phase. A more likely reaction is the cleavage of a C−N bond to form CH_2NNO_2 and INT4, with a barrier of 24.7 kcal/mol, followed by further dissociation of INT4, as depicted in Figure 6.

$$\text{RDR-N} \rightarrow \text{RDR-No} \rightarrow \text{CH}_2\text{NNO}_2 + \text{INT4} \tag{8a}$$

$$\text{INT4} \rightarrow \text{CH}_2\text{NNO}_2 + \text{CH}_2\text{N} \tag{8b}$$

CH_2NNO_2 can undergo homolysis to produce CH_2N and NO_2

$$\text{CH}_2\text{NNO}_2 \rightarrow \text{CH}_2\text{N} + \text{NO}_2 \tag{9}$$

NO_2 produced in this way will have low internal energy and can produce LW emission.

TABLE 3: Activation Barriers and Backward Barriers for Unassisted and Radical Assisted N−N Homolysis of RDX (All Energies in kcal/mol)

	reaction	forward barrier	backward barrier
RDX homolysis	RDX → RDR-N + NO_2	38.9	
radical assisted homolysis	RDX + HCNH→ RDR-N + $CH(NO_2)NH$	20.8	38.4
	RDX + CH_2N → RDR-N + CH_2NNO_2	35.7	28.5
	RDX + OH → RDR-N + HNO_3	25.5	35.4
	RDX + NO → RDR-N + N_2O_3	36.9	7.2

To this point, the decomposition is unimolecular and leads to the production of various fragments, notably HONO, which gives UV emission, and NO_2, which can emit in both the VIS and LW regions of the spectrum. This is consistent with the emission spectra observed in low stress, shock wave experiments.[1]

Decomposition at High Stress: Mechanism for Acceleration. In the high stress shock experiments, the emission spectrum initially resembled that of the low stress experiments. From this, we conclude that the initial decomposition follows the unimolecular pathways previously outlined. Above the threshold, however, the LW component dominated the spectrum. This spectral change was accompanied by an increase in total emission intensity, suggesting accelerated decomposition. We proposed that this acceleration may be due to bimolecular reactions between radical products and unreacted RDX molecules.[1]

The unimolecular decomposition pathway produces multiple radical species. These radicals can interact with RDX in several ways. It is important, however, that these reactions lead to the production of RDR-N. As we have shown, RDR-N tends to open the ring. As decomposition proceeds, more radicals are produced. We propose a radical assisted homolysis reaction to remove NO_2 from RDX to produce RDR-N.

$$\text{Radical} + \text{RDX} \rightarrow \text{Rad-NO}_2 + \text{RDR-N} \qquad (10)$$

We calculated activation barriers for several different radicals reacting with RDX. These results are shown in Table 3. As an example of this process, the reaction between HCNH and RDX is depicted in Figure 7.

$$\text{HCNH} + \text{RDX} \rightarrow \text{RDR-N} + \text{HC(NO}_2\text{)NH} \qquad (10')$$

The barrier was determined to be 20.8 kcal/mol, compared to 38.9 kcal/mol for unassisted N−N homolysis. This reaction has an exothermic back barrier of 38.4 kcal/mol, whereas the unassisted homolysis reaction has no back barrier. Because the attacking radical forms a stable molecule with the NO_2 group, it stabilizes the products of the homolysis. HCNH is produced from CH_2N through isomerization.

$$\text{CH}_2\text{N} \rightarrow \text{HCNH} \qquad (11)$$

OH and NO radicals can be produced through dissociation of HONO. Regardless of the actual radical species involved, radical assisted homolysis leads to formation of RDR-N. RDR-N then decomposes as already discussed, leading to the formation of more radical products that accelerate the decomposition. We expect the preexponential factor for any bimolecular process to be significantly smaller than for a unimolecular process. Thus, this pathway can only become operative once a sufficient concentration of radicals has been produced. The confinement provided by the solid state of the RDX crystal may aid these processes.

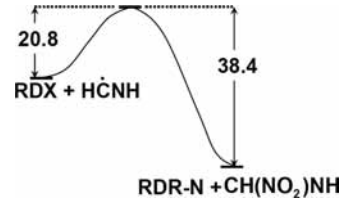

Figure 7. Potential energy profiles for bimolecular reaction: carbon radical (HCNH) subtracts NO_2 from RDX. Energy given in kcal/mol.

A prior study reported that the C−H bond of RDX is weak, and suggested that radical abstraction of hydrogen from RDX could propagate the decomposition.[6] We calculated the barrier for the following reaction and found it to be 28.5 kcal/mol.

$$\text{Rad} + \text{RDX} \rightarrow \text{Rad-H} + \text{RDR-C2} \qquad (12)$$

However, RDR-C2 can release NO_2 to form INT1.

$$\text{RDR-C2} \rightarrow \text{INT1} + \text{NO}_2 \qquad (13)$$

Our calculations found no barrier for this reaction. INT1 is the same product as from the HONO elimination mechanism and does not participate further in the scheme. This process allows the radical decomposition to propagate but does not accelerate decomposition. Thus, C-centered radicals, such as RDR-C and RDR-C2, are not the primary species that accelerate the decomposition. NO_2 produced in this fashion could, however, contribute to the VIS portion of the spectrum.

We propose the following mechanism for the acceleration of decomposition above the threshold observed in our experiments. The energy and concentration of free radicals increase in response to high pressure over time resulting in bimolecular reactions between free radicals and neighboring RDX molecules. The RDX molecules undergo radical assisted homolysis reactions to release NO_2 and form RDR-N. RDR-N then undergoes ring opening and further decomposition to produce CH_2NNO_2, which itself decomposes to produce NO_2 capable of producing LW emission and the CH_2N radical. Once this bimolecular reaction channel becomes operative, it will accelerate the decomposition of RDX, and the unimolecular pathways contribute less to the total decomposition. For this reason, the LW component dominates the emission spectrum.

Decomposition Scheme. Figure 8 depicts our proposed decomposition scheme for shock wave induced decomposition of RDX, consistent with the experimental observations.[1] Under low shock stress, HONO elimination (reaction 2) leads to the observed UV emission. HONO elimination produces INT1, which does not participate further in the decomposition scheme. Reaction 4 leads to the production of RDR-C, which eliminates NO_2 that emits in the VIS region (reaction 5). N−N homolysis, reaction 1, produces NO_2 that can produce LW emission and the N-centered radical RDR-N. RDR-N can react in a few different pathways. H migration without ring opening (reaction 6), produces the C-centered radical, RDR-C. However, ring opening of RDR-N (8) is preferred. This pathway leads to the production of CH_2NNO_2, which further decomposes to give NO_2 and CH_2N (9). The NO_2 produced by this reaction can contribute to LW emission.

The early stages of decomposition produce all three emission components, as observed in the shock experiments. It should be noted that the time scale of the shock experiment does not permit us to observe these reactions in sequence. Only the

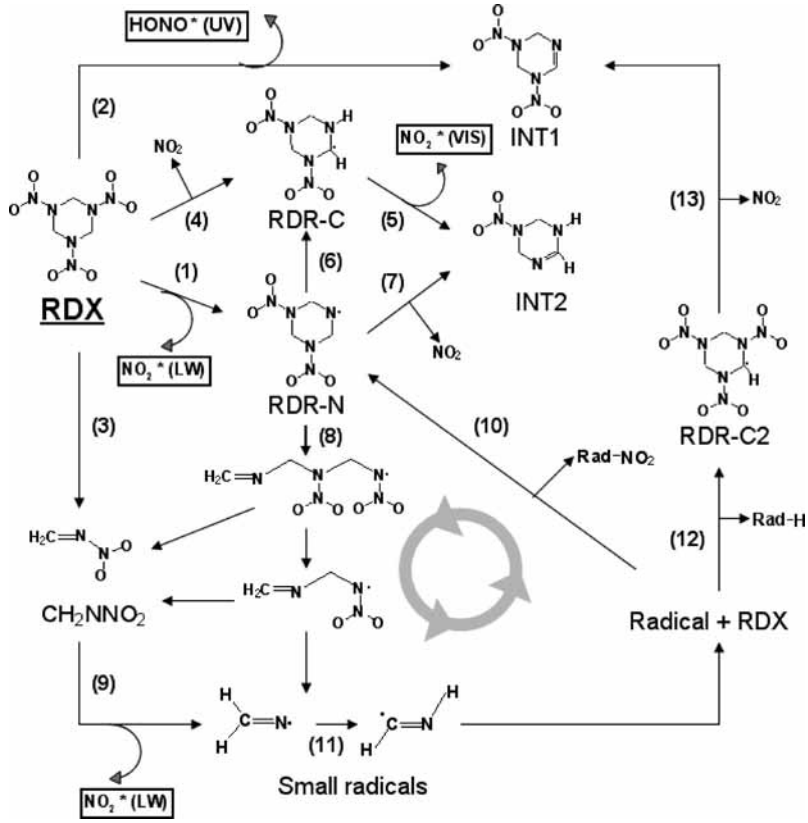

Figure 8. Initial chemical steps of shock-wave induced decomposition of RDX crystal.

cumulative effect can be observed. The experimentally observed emission components can be connected to the chemical reactions as follows:

UV	(2)
VIS	(4) → (5) or
	(1) → (6) → (5)
LW	(1) → (8) → (9)

When peak stress is above the 10 GPa threshold, the system initially reacts through the unimolecular decomposition channels until the radical products are sufficiently abundant for bimolecular free radical reactions. Radical assisted homolysis (10) of unreacted RDX molecules leads to the production of RDR-N, which will then undergo ring opening and fragmentation. The radical intermediates then react with neighboring RDX molecules to accelerate the decomposition. Once this channel becomes active, the contribution of unimolecular pathways to decomposition decreases. NO_2 will be produced mainly in the B_2 excited state and LW emission dominates the spectrum. The experimentally observed emission is connected to the chemical reactions in this fashion.

LW (10) → (8) → (9) → (10)

For the highest peak stress experiment, 20 GPa, LW emission dominated the spectrum even in early decomposition. This suggests that the bimolecular pathway opened up very early, through the sequences outlined above. Some light was detected for the other emission components, suggesting that unimolecular decomposition still takes place under these conditions. Once there is sufficient reaction to be observed by the detection system, the decomposition has already progressed to the later stages.

An alternative pathway involves direct ring dissociation of RDX through reaction 3. It is possible that the stress and temperature conditions in this experiment overcame the activation energy barrier and negated the constraints of the activation volume. This reaction leads to direct production of three CH_2NNO_2 molecules, which can then decompose to CH_2N and NO_2 that gives rise to the emission spectrum dominated by the LW component. The produced radicals can start the bimolecular reactions and further contribute to the LW component of the emission spectrum. This channel is summarized in this way.

LW (3) → (9) → (10) → (8) → (9) → (10) ...

We reemphasize that the above decomposition scheme is based on calculations for isolated molecules. This qualitative scheme accounts for the observed profile of the emission spectrum and its dependence on time and shock stress. In the crystalline environment, the activation energy and volume of these decomposition reactions may change under elevated temperature and pressure. The full examination of these effects goes beyond the scope of this paper. However, because the covalent bonding features of RDX molecule and its decomposition intermediates remain, these changes should not be large enough to alter the preference of decomposition pathways and therefore would not invalidate the proposed decomposition scheme.

V. Concluding Remarks

We have proposed a scheme for the shock induced chemical decomposition of RDX based on experimental observations and quantum chemistry calculations. HONO and NO_2 are proposed as the emitting intermediates observed in the experiments. NO_2 is produced through multiple chemical pathways and the profile of the emission spectrum changes in time. Homolysis of RDX

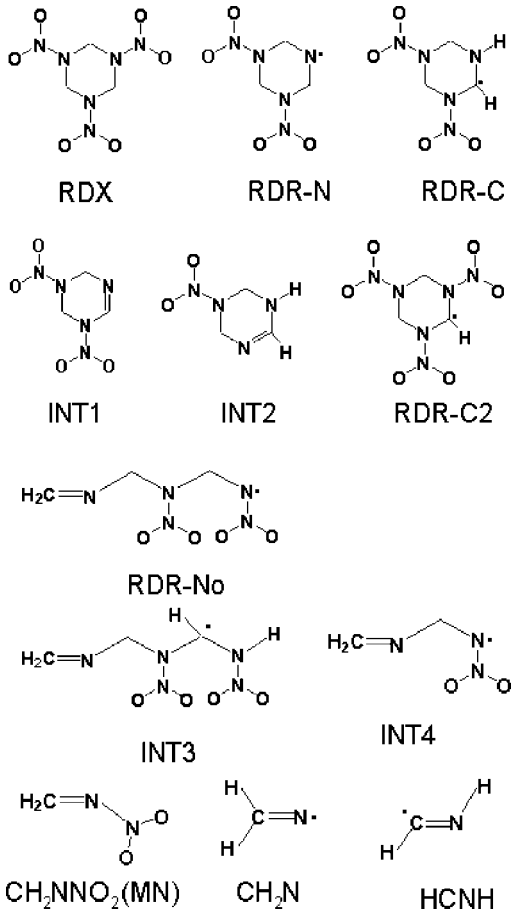

Figure A1. RDX and various decomposition intermediates and products.

produces a N-centered radical (RDR-N) that leads to further decomposition and the production of small radicals. This unimolecular decomposition scheme accounts for all the features observed in the low stress shock experiments and in the early stage of the high stress experiments.

At a later time in the experiments above the 10 GPa threshold, the long wavelength component dominates the spectrum. This is due to the onset of bimolecular reactions between free radical products and unreacted RDX that accelerate the decomposition. Specifically, radical assisted homolysis leads to RDR-N, which continues the decomposition cycle.

Unlike previously proposed decomposition schemes, ours is based on the results of real-time measurements of shock-induced emission spectra. The time scale of the experiments is a few hundred nanoseconds, compared to the much longer time scales of most previous experiments. Short-lived intermediates could not be observed due to their participation in secondary reactions.

It should also be noted that we have not discussed how the energy couples from the shock wave to the molecule to initiate the decomposition. Several mechanisms for this energy transfer have been put forward,[32–35] but such a discussion is beyond the scope of this work. Finally, our results and proposed decomposition scheme are relevant only to the initial stages of shock induced decomposition prior to the development of a detonation wave. Additional chemical pathways likely play a role once detonation conditions are realized.

Acknowledgment. This work was supported by ONR MURI Grants N00014-01-1-0802 and N00014-06-1-0459, and DOE Grant DEFG0397SF21388.

Appendix

Figure A1 contains the structures of several decomposition intermediates included in the proposed scheme.

References and Notes

(1) Patterson, J. E.; Dreger, Z. A.; Miao, M.; Gupta, Y. M. *J. Phys. Chem. B* **2008**, *112*, 7374.
(2) Melius, C. F. In *Chemistry and Physics of Energetic Materials*; Bulusu, S. N., Ed.; Kluwer Academic Publishers: Amsterdam, 1990; Vol. 309, pp 21.
(3) Habibollahzadeh, D.; Grodzicki, M.; Seminario, J. M.; Politzer, P. *J. Phys. Chem.* **1991**, *95*, 7699.
(4) Sewell, T. D.; Thompson, D. L. *J. Phys. Chem.* **1991**, *95*, 6228.
(5) Farber, M. *Mass Spectrom. Rev.* **1992**, *11*, 137.
(6) Harris, N. J.; Lammertsma, K. *J. Am. Chem. Soc.* **1997**, *119*, 6583.
(7) Wu, C. J.; Fried, L. E. *J. Phys. Chem. A* **1997**, *101*, 8675.
(8) Shalashilin, D. V.; Thompson, D. L. *J. Phys. Chem. A* **1997**, *101*, 961.
(9) Chakraborty, D.; Muller, R. P.; Dasgupta, S.; Goddard, W. A., III *J. Phys. Chem. A* **2000**, *104*, 2261.
(10) Strachan, A.; van Duin, A. C. T.; Chakraborty, D.; Dasgupta, S.; Goddard, W. A. *Phys. Rev. Lett.* **2003**, 91. 098301/1.
(11) Strachan, A.; Kober, E. M.; van Duin, A. C. T.; Oxgaard, J.; Goddard, W. A. *J. Chem. Phys.* **2005**, *122*, 054502/1.
(12) Davidson, A. J.; Oswald, I. D. H.; Francis, D. J.; Lennie, A. R.; Marshall, W. G.; Millar, D. I. A.; Pulham, C. R.; Warren, J. E.; Cumming, A. S. *CrystEngComm* **2008**, *10*, 162.
(13) Shishkov, I. F.; Vilkov, L. V.; Kolonits, M.; Rozsondai, B. *Struct. Chem.* **1991**, *2*, 57.
(14) Lee, C.; Yang, W.; Parr, R. G. *Phys. Rev. B: Condens. Matter Mater. Phys.* **1988**, *37*, 785.
(15) Becke, A. D. *J. Chem. Phys.* **1992**, *97*, 9173.
(16) Becke, A. D. *J. Chem. Phys.* **1992**, *96*, 2155.
(17) Becke, A. D. *J. Chem. Phys.* **1993**, *98*, 5648.
(18) Frisch, M. J. T., G. W.; Schlegel, H. B.; Scuseria, G. E.; Robb, M. A.; Cheeseman, J. R.; Montgomery, J. A., Jr.; Vreven, T.; Kudin, K. N.; Burant, J. C.; Millam, J. M.; Iyengar, S. S.; Tomasi, J.; Barone, V.; Mennucci, B.; Cossi, M.; Scalmani, G.; Rega, N.; Petersson, G. A.; Nakatsuji, H.; Hada, M.; Ehara, M.; Toyota, K.; Fukuda, R.; Hasegawa, J.; Ishida, M.; Nakajima, T.; Honda, Y.; Kitao, O.; Nakai, H.; Klene, M.; Li, X.; Knox, J. E.; Hratchian, H. P.; Cross, J. B.; Bakken, V.; Adamo, C.; Jaramillo, J.; Gomperts, R.; Stratmann, R. E.; Yazyev, O.; Austin, A. J.; Cammi, R.; Pomelli, C.; Ochterski, J. W.; Ayala, P. Y.; Morokuma, K.; Voth, G. A.; Salvador, P.; Dannenberg, J. J.; Zakrzewski, V. G.; Dapprich, S.; Daniels, A. D.; Strain, M. C.; Farkas, O.; Malick, D. K.; Rabuck, A. D.; Raghavachari, K.; Foresman, J. B.; Ortiz, J. V.; Cui, Q.; Baboul, A. G.; Clifford, S.; Cioslowski, J.; Stefanov, B. B.; Liu, G.; Liashenko, A.; Piskorz, P.; Komaromi, I.; Martin, R. L.; Fox, D. J.; Keith, T.; Al-Laham, M. A.; Peng, C. Y.; Nanayakkara, A.; Challacombe, M.; Gill, P. M. W.; Johnson, B.; Chen, W.; Wong, M. W.; Gonzalez, C.;and Pople, J. *A. Gaussian 03*, revision D.01; Gaussian, Inc.: Wallingford, CT, 2004.
(19) Levitt, B. P. *J. Chem. Phys.* **1965**, *42*, 1038.
(20) Inoue, G.; Nakata, Y.; Usui, Y.; Akimoto, H.; Okuda, M. *J. Chem. Phys.* **1979**, *70*, 3689.
(21) Gillispie, G. D.; Khan, A. U.; Wahl, A. C.; Hosteny, R. P.; Krauss, M. *J. Chem. Phys.* **1975**, *63*, 3425.
(22) Gillispie, G. D.; Khan, A. U. *J. Chem. Phys.* **1976**, *65*, 1624.
(23) Douglas, A. E. *J. Chem. Phys.* **1966**, *45*, 1007.
(24) Haller, E.; Koeppel, H.; Cederbaum, L. S. *J. Mol. Spectrosc.* **1985**, *111*, 377.
(25) Adler-Golden, S. M. *J. Phys. Chem.* **1989**, *93*, 691.
(26) Choi, C. S.; Prince, E. *Acta Crystallogr.* **1972**, *B28*, 2857.
(27) Reviewed in the introduction to the companion paper, preceding paper this issue.
(28) Goto, N.; Fujihisa, H.; Yamawaki, H.; Wakabayashi, K.; Nakayama, Y.; Yoshida, M.; Koshi, M. *J. Phys. Chem. B* **2006**, *110*, 23655.
(29) Dreger, Z. A.; Gupta, Y. M. *J. Phys. Chem. B* **2007**, *111*, 3893.
(30) Wight, C. A.; Botcher, T. R. *J. Am. Chem. Soc.* **1992**, *114*, 8303.
(31) Adams, G. F.; Shaw, R. W. *Annu. Rev. Phys. Chem.* **1992**, *43*, 311.
(32) Dlott, D. D.; Fayer, M. D. *J. Chem. Phys.* **1990**, *92*, 3798.
(33) Gilman, J. J. *Philos. Mag. B* **1995**, *71*, 1057.
(34) Coffey, C. S. In *Theoretical and Computational Chemistry*; Politzer, P. A., Murray, J. S., Eds.; Elsevier: Amsterdam, The Netherlands, 2003; Vol. 13, pp 101.
(35) Kuklja, M. M. *Appl. Phys. A: Mater. Sci. Processing* **2003**, *76*, 359.

JP8008282